RESEARCH ARTICLE | SEPTEMBER 25 2024

Capillary wave-assisted collapse of non-Newtonian droplets



Ziwen He (10); Huy Tran (10); Min Y. Pack (12)



Physics of Fluids 36, 092127 (2024) https://doi.org/10.1063/5.0231029

A CHORUS





Articles You May Be Interested In

Dual nature of volatility on drop wetting dynamics of acetone—isopropanol mixtures on ultrathin smooth oil films

Physics of Fluids (January 2023)

Motor characteristics determine the rheological behavior of a suspension of microswimmers

Physics of Fluids (July 2014)

Air entrainment dynamics of aqueous polymeric droplets from dilute to semidilute unentangled regimes

Physics of Fluids (November 2022)



Physics of Fluids

Special Topics Open for Submissions

Learn More



Capillary wave-assisted collapse of non-Newtonian droplets

Cite as: Phys. Fluids **36**, 092127 (2024); doi: 10.1063/5.0231029 Submitted: 28 July 2024 · Accepted: 7 September 2024 · Published Online: 25 September 2024







Ziwen He,^{1,2} 🕞 Huy Tran,² 🕞 and Min Y. Pack^{2,a)} 🕞

AFFILIATIONS

- ¹Department of Chemical Engineering and Materials Science, University of Minnesota, Minneapolis, Minnesota 55455, USA ²Department of Mechanical Engineering, Baylor University, Waco, Texas 76798, USA
- a) Author to whom correspondence should be addressed: Min Pack@baylor.edu

ABSTRACT

Understanding the peripheral capillary wave propagation during droplet impact is crucial for comprehending the physics of wetting onset and droplet fragmentation. Although Newtonian droplets have been extensively studied, we show how capillary waves deform non-Newtonian droplets in such a way that rheological features, such as the critical concentrations for the overlap (c^*) and entangled polymer molecules (c^{**}), may be directly obtained from the deformation history. Determining these critical concentrations is essential as they mark transitions in the rheological behavior of aqueous polymeric solutions, influencing viscosity, elasticity, and associated fluid dynamics. We have also compared capillary waves among Newtonian, shear-thinning, and Boger fluid droplets and found that although the fluid kinematics appear to be purely biaxial extensional flow, the infinite-shear properties of the droplets dominate the physics of capillary wave formation and propagation.

Published under an exclusive license by AIP Publishing. https://doi.org/10.1063/5.0231029

I. INTRODUCTION

A variety of applications depend on the precise control of the droplet deposition dynamics, such as in inkjet printing, 1,2 agrochemical deposition,³ spray coating,⁴ and respiratory droplet dispersal⁵—many of which involve non-Newtonian fluids. Droplet wetting is initiated when the approaching droplet thins the ambient fluid down to length scales relevant for intermolecular forces to drive contact. In air, the thin film failure occurs within the range of O(1 nm) to O(100 nm), as revealed by various techniques such as interferometry (RIM)^{6–8} and total internal reflection microscopy (TIRM).9-13 At sufficiently low capillary numbers, $Ca = \eta U/\gamma$, where η is the liquid viscosity, U is the impact velocity, and γ is the surface tension, the impulse triggers capillary waves at the basal plane, leading to an amplification of the waves at the apex and then to a final reentrant jet, which may assist in overcoming the viscous resistance at the basal plane (i.e., lubrication force due to the entrapped air film) and initiate wetting 14 or form a dry spot 15 after the air layer ruptures. Previous studies have also shown that the rapid closure of the cavity from the reentrant jet may form another jet, which could release satellite droplets. 16,17 Consequently, the control of deposition dynamics in wetting inception and droplet breakup is intricately tied to peripheral capillary wave propagation.

In order to control the wetting dynamics of droplets, previous studies have utilized the addition of polymers to promote droplets to stick to surfaces,¹⁸ where it has been previously proposed that the increase in the first normal stress difference during the retraction phase counteracted capillarity.¹⁹ The role of the extensional viscosity has remained ambiguous as some studies have downplayed its significance^{20,21} while others have suggested the importance of extensional effects due to the large strain rates, \dot{e} , experienced during impact across the dilute to entangled polymer concentrations.^{11,12,22–24} Despite the existing literature on the non-Newtonian droplet impact dynamics, the relative importance of shear and extensional effects remains unclear.

In this study, we investigated the roles of shear and extensional effects in the capillary wave-induced collapse of non-Newtonian droplets. We separated the shear effects from the elastic effects by comparing droplet impact with strongly shear-thinning solutions, Xanthan gum (XG, MW ≈ 2.7 MDa), and a Boger fluid where the viscosity is independent of shear rate. The Boger fluid was made by mixing polyethylene oxide (PEO, MW ≈ 4 MDa) and polyethylene glycol (PEG, MW ≈ 8000 Da). Using the combined RIM-TIRM technique, we highlighted the significance of rheological properties in altering the central collapse dynamics of non-Newtonian droplets and provided a droplet-based method for the rapid detection of rheological features such as c^* and c^{**} , for polymer solutions with low volume consumption.

In the experiments, the G/W solution with 78 wt. % glycerol effectively suppressed capillary waves on the droplet surface, leading to a matched zero-shear viscosity, η_0 , of approximately 50 mPa s among G/W 78 wt. %, Boger, and XG 250 ppm solutions. Comparing the

Newtonian, Boger, and XG droplets during the deformation as shown in Figs. 1(c)–1(e), the dynamics revealed the observation of capillary waves on the XG droplets only, emphasizing the significance of the shear-thinning response induced by the peripheral motion of the capillary waves. Consequently, capillary waves concentrated at the apex $(t/t_{\rm ic}=0.69,$ where $t_{\rm ic}=\sqrt{\rho R^3/\gamma})$ on the XG 250 ppm droplets and eventually formed a reentrant jet at around $t\approx 4.7$ ms $(t/t_{\rm ic}=1.08)$, leading to a dimple inversion revealed by RIM and TIRM techniques [see red dashed circles in Figs. 1(b) and 1(d)]. The dimple inversion appeared as a dark region (intensity decrease) at the center of the air layer detected by the TIRM and the vanishing of interference fringes as detected by the RIM, indicating a sudden and significant decrease in the central distance between the droplet and the substrate (viscous oil film), causing central wetting of the droplets at sufficiently large collapse rates. 11,13

II. EXPERIMENTAL METHODS

A. Droplet impact dynamics

1. Droplet impact setup

Droplets of glycerol–water (G/W) mixtures with varying glycerol concentrations (10, 31, 52.3, 78 wt. %), XG (5–10 000 ppm), and Boger (PEO 0.4 wt. %/PEG 15 wt. %) solutions were dispensed from a needle driven by a syringe pump at a flow rate of 1 ml/hr. The droplet sizes R were determined by averaging measurements from at least three

in-flight droplets for each solution per impact height, ranging from 1.02 ± 0.02 to 1.12 ± 0.04 mm due to the slight change in surface tension by adding polymer additives. The liquid density ρ was measured using a pycnometer with no significant changes in the solution densities. The impact velocity U was adjusted by varying the release height of the droplet to the substrate, resulting in a range of Weber numbers $(We = \rho U^2 R/\gamma)$ from 2 to 10. The droplet impact and its peripheral capillary wave propagation were recorded using shadowgraphy with a Phantom high-speed camera (V211) operating at a frame rate of 8000 fps as shown in the top row of Figs. 1(c)-1(e) (Multimedia available online). To eliminate asperity-induced random droplet collapse, the glass slide was spin-coated with a thin layer of silicone oil ($\eta_{\rm oil}\approx 1080$ mPa s) with a thickness of approximately 2 μ m. This coating preserved the dynamics of the intervening air layer while minimizing the deformation of the oil film. $^{11-13,26}$ The entire droplet impact setup was enclosed in a custom-built chamber where the relative humidity and temperature were tracked. The temperature was nearly a constant at 20 ± 0.1 °C and the relative humidity was $31.2 \pm 2.3\%$.

2. Air layer measurement: Combined RIM-TIRM technique

The combined RIM-TIRM technique provided the bottom view, enabling the characterization of the intervening air layer during

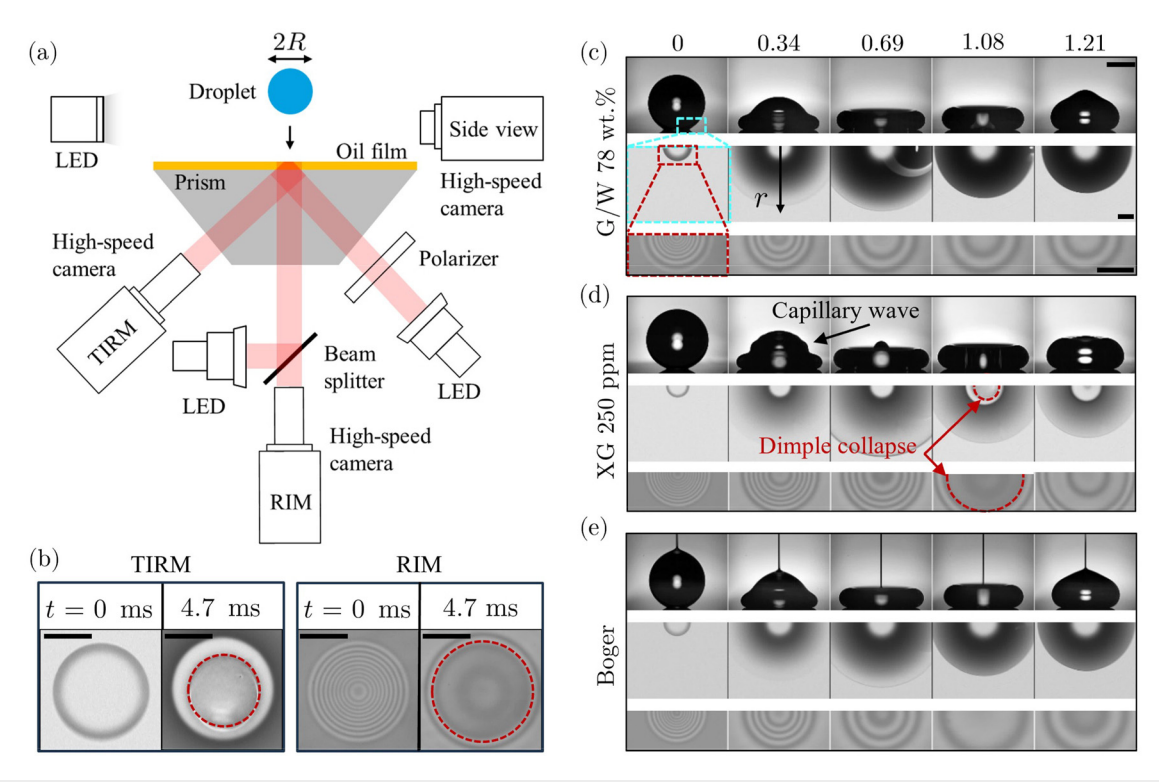


FIG. 1. (a) A schematic of the combined RIM-TIRM technique and the droplet impact setup (not to scale). The side-view impact was captured using a 150-W AmScope fiber optic light or a Phlox light emitting diode (LED) panel and the bottom views (RIM and TIRM) were illuminated by collimated LED with a wavelength of 625 nm. (b) Snapshots of dimple collapse from RIM and TIRM highlighted by the red dashed circle. t=0 ms is defined as when the high-speed camera first observed the air dimple and t=4.7 ms is selected when the dimple experiences the greatest collapse. Droplet deformation (top row) and the corresponding evolution of the air layer morphologies captured by TIRM (middle row) and RIM (bottom row) for (c) G/W 78 wt. %, (d) XG 250 ppm, and (e) Boger droplets at We ≈ 5 , where the time is normalized by the inertio-capillary timescale, $t_{\rm fc} = \sqrt{\rho R^3/\gamma}$. The scale bar represents 0.5 mm. Multimedia available online.

droplet impact. For RIM measurements, a monochromatic LED light with a wavelength of 625 nm (ThroLabs M625L4) was used to illuminate the droplet-air interface through the substrate vertically. A highspeed camera (Phantom V211) operating at 25 000 fps with a $5 \mu s$ exposure time connected to a 5× objective was used to capture the interference patterns created by the reflected light from the droplet-air interface and the air-oil interface, as shown in the bottom row of Figs. 1(c)-1(e) (Multimedia available online). The fringe-to-fringe spacing results in either an increase or a decrease in the gap height in multiples of half of the wavelength utilized. The gradient in the air gap thickness is set by the amplitude of the intensity changes, where the decrease in the amplitude results in larger gaps and increase in the amplitude results in smaller gap thickness. The TIRM setup involved creating an exponentially decaying wave (evanescent wave) above the oil-air interface, which was induced by the total internal reflection of a collimated p-polarized incident LED light beam, by illuminating the interface at an incident angle (i.e., ≈49.92°, which is greater than the critical angle of 45.6° for oil-air interfaces). When the droplet enters the evanescent wave region, the reflected light was frustrated due to the higher refractive index of the droplet than air, causing an intensity decrease (circular shades captured by the camera). A TIRM snapshot of droplet impact is shown in the middle row of Figs. 1(c)-1(e) (Multimedia available online). Further details of TIRM imaging including the height extraction can be found in previous studies. 11,14 Overall, we implemented the combined RIM-TIRM to probe the complementary detail of dimple inversion induced by the top surface collapse, where the TIRM measured the air layer thickness up to (≈600 nm), while the RIM allows the measurement to obtain the relative air layer thickness between (\approx 150 nm) and several micrometers (\approx 3 μ m).

B. Rheological characterization

The rheology of the polymeric droplets was measured using a rheometer (Anton Paar MCR 302e) equipped with a cone-plate geometry (diameter 59.976 mm, angle 0.986°) and a double-gap spindle (DG26.7). Flow curves and the first normal stress difference were measured by the cone-plate geometry. The spindle measured oscillatory measurements such as amplitude and frequency sweep owing to its higher accuracy in low torque regions with more contact surface area compared with the cone-plate geometry. The temperature was kept at a constant 20.0 \pm 0.1 °C. Serial dilution was performed for the preparation of all samples which were gently stirred at 80 rpm for at least 24 h. The solvent was de-ionized water with a resistivity of 18.2 $M\Omega$ cm $^{-1}$ (MilliporeSigma). During the rheological measurements, all solutions were pre-sheared with a shear rate of $\dot{\gamma}=10~\text{s}^{-1}$ for 2 min and allowed for another 2 min to fully relax. In addition, the measuring region was enclosed by a custom-built cover to limit solvent evaporation.

1. Shear rheology

The shear viscosity was obtained by applying a shear rate ramping up from 0.1 to $1000\,\mathrm{s^{-1}}$, which exhibits rate-independent behavior at low concentrations for both XG and PEO solutions. As the concentration surpassed the critical overlap concentration c^* , the increase in the shear viscosity became more pronounced but displayed thinning behavior over the shear rate. This thinning response was presumably due to the alignment of polymer molecules under shear flow. The rate-dependent variation of shear viscosity was described by the Carreau-Yasuda model [Eq. (1)] for all the test fluids as illustrated in Figs. 2(a) and 2(b).

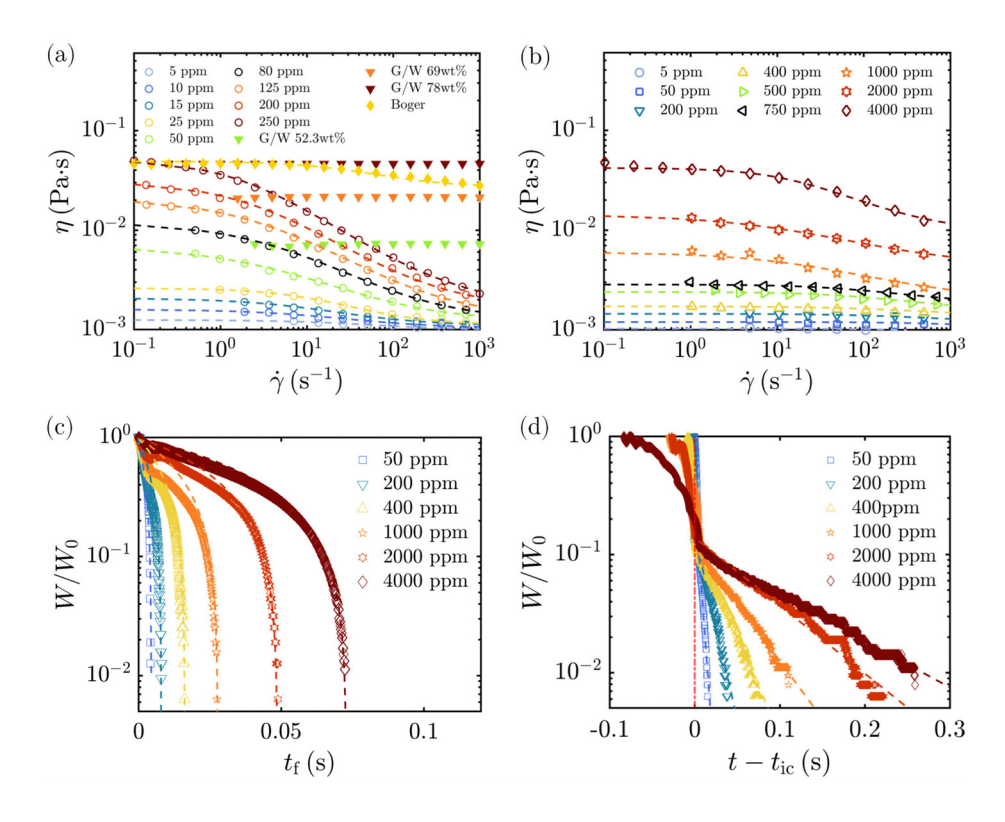


FIG. 2. (a) Shear viscosity of the XG, G/ W, and Boger solutions, as well as (b) PEO solutions. The viscosity was measured using a cone-plate geometry. Dashed lines are the Carreau-Yasuda model fitted onto XG and PEO and Boger solutions. Filament thinning dynamics the dripping-onto-substrate method.²⁵ (c) The filament of XG solutions reduced following a power law and was fitted by the single-mode Giesekus model [Eq. (3)]. (d) PEO solutions fitted by Eq. to the linear regime beyond inertiocapillary timescale marked by the red dotdashed line, $t_{\rm ic}$, where $t_{\rm f}-t_{\rm ic}=0$ sets the onset of the elasto-capillary regime.

$$\frac{\eta - \eta_{\infty}}{\eta_0 - \eta_{\infty}} = \left[1 + \left(K\dot{\gamma}\right)^m\right]^{\frac{n-1}{m}},\tag{1}$$

where η_0 is the zero-shear viscosity, η_{∞} is the infinite-shear viscosity measured at $1000 \, \text{s}^{-1}$, K is the time constant, n the power law index, and the constant m describes the transition between Newtonian and power-law regions.

The first normal stress difference, N_1 , of XG 250 ppm and the Boger solution was compared by measuring the frequency sweep and the corresponding elastic modulus. At high shear rates ($\dot{\gamma} > 300 \text{ s}^{-1}$), the Boger solution exhibited larger N_1 due to the higher elasticity (see the inset in Fig. 3). A three order of magnitude difference in N_1 was detected between the Boger and XG 250 ppm solutions at 1000 s^{-1} .

2. Extensional rheology

The extensional properties were measured using the drippingonto-substrate (DoS) method²⁵ by depositing polymeric solutions onto a cleaned glass slide and observing the thinning dynamics of the filament. For PEO solutions, the thinning dynamics was captured by the following expression:²⁸

$$\frac{W}{W_0} \approx \frac{G'W_0}{2\gamma} \exp\left(-\frac{t}{3\tau_e}\right),$$
 (2)

where W is the filament diameter, W_0 is the initial diameter, G' is the elastic modulus, and τ_e is the apparent uniaxial relaxation time, which can be extracted from the semi-log plot by fitting to the elasto-capillary regime as shown in Fig. 2(d).

The Giesekus model for uniaxial flow was used to describe the power-law thinning dynamics of XG solutions:

$$\frac{\sigma_{zz}}{\tau_e} + \frac{5\gamma}{W^2} \frac{dW}{dt} + \frac{k}{\eta(\dot{\gamma})} \sigma_{zz}^2 = -\frac{4\eta(\dot{\gamma})}{\tau_e} \frac{1}{W} \frac{dW}{dt}, \tag{3}$$

where σ_{zz} is the axial stress related to the capillary stress driving the pinch-off, k is the mobility parameter, and $\eta(\dot{\gamma})$ is the effective shear viscosity at 4.7 s⁻¹, which accounts for the shear from the inner surface of the needle under a flow rate of 1 ml/h with a needle diameter of

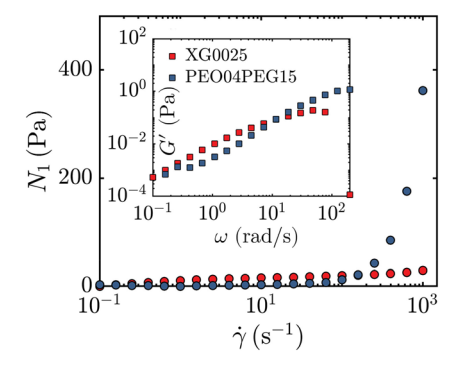


FIG. 3. The first normal stress difference N_1 indicates that the Boger solution exhibited a thrust three order of magnitude greater than that of XG 250 ppm at a high shear rate of $1000 \, \text{s}^{-1}$. Inset: Elastic modulus of XG 250 ppm and Boger droplets over angular frequencies.

TABLE I. Parameters of the single-mode Giesekus model for XG solutions.

c (ppm)	k	$\eta(\dot{\gamma})$ (Pa s)	τ _e (s)
50	0.0156	0.0014	0.35
250	0.035	0.0051	0.42
400	0.048	0.0133	0.46
1000	0.132	0.0603	0.49
2000	0.208	0.163	0.58
4000	0.413	0.484	0.63

0.838 mm. Table I summarizes the parameters used in the Giesekus model for various concentrations of XG solutions.

III. RESULTS AND DISCUSSION

During an impact experiment, capillary waves formed and propagated from the bottom of the spreading droplet over time, as depicted in Fig. 4 (Multimedia available online). At $t=3.52\,\mathrm{ms}$, the top surface overturned at a velocity of U_T and formed a toroidal shape at $t=4.24\,\mathrm{ms}$. A reentrant jet was created by the inverted top surface and was visualized by a green laser sheet (about 3 mm long and 0.25 mm wide) with a wavelength of \approx 532 nm after passing through a cylindrical lens. By illuminating the cross section of the droplet, a Photron high-speed camera (Nova S9) with frame rates varying from 25 000 to 50 000 fps was used to directly track the top surface motion and measure U_T . The measured U_T , which was found to be close to the impact velocity of the droplet, is also discussed elsewhere. ¹¹

As the reentrant jet is influenced by the focusing of capillary waves at the droplet apex, we first examined the propagation dynamics of these waves along the droplet surface. Figure 5(a) illustrates the movement of the capillary waves along the droplet-air interface in a polar coordinate system (r, ϕ) , with the origin $(r = 0, \phi = 0)$ located at the droplet center before the deformation at t = 0. Our analysis focused on the time period when $t \ge 0.08$ ms, during which the

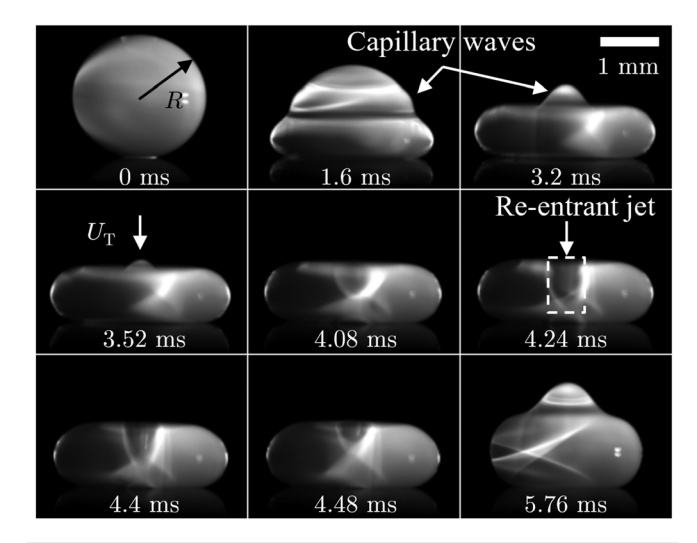


FIG. 4. Reentrant jet induced by capillary-wave collapse at We \approx 2.5 of the XG 250 ppm droplet. Multimedia available online.

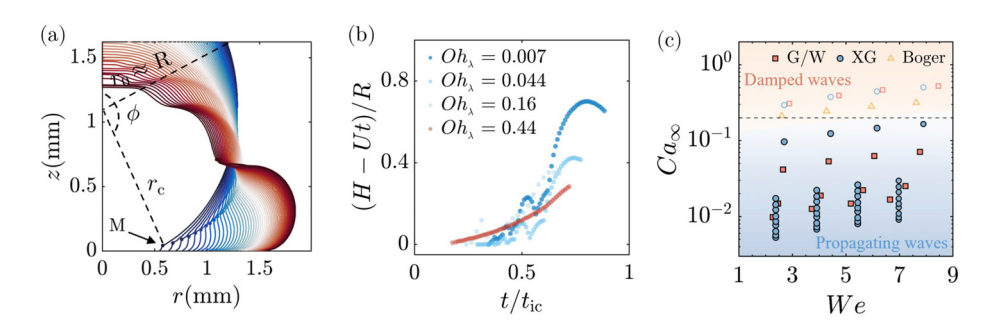


FIG. 5. (a) The deformation of a XG 250 ppm droplet over time after impacting the substrate at $We \approx 5$. The solid point M tracks the primary wave and the spreading bottom. (b) The interfacial perturbation at the apex of the drop as a function of the normalized time utilizing the inertio-capillary timescale. (c) Regime map of the capillary waves for all solutions. Solid data points represent the propagating capillary waves and hollow represent the damped waves. The dashed line represents $Ca_{cr} = 0.2$.

primary wave became visible through our optics. This wave, marked by point M [see Fig. 5(a)], was found to be responsible for overturning the top surface, which led to the formation of the reentrant jet. The wave tracking at M was possible by tracking the angular and radial changes in ϕ and r_c , respectively.

For capillary waves induced by droplet impact, a characteristic length scale can be obtained by using the impact velocity of the droplet as the phase velocity of the maximal wave, ¹⁵

$$\lambda = \gamma/(\rho U^2). \tag{4}$$

We thus estimate the local shear rate near the perturbed surface as $\dot{\gamma}_{\rm c} \approx 2U/\lambda > 1000~{\rm s}^{-1}$ and consider η_{∞} as the effective viscosity that attenuates the capillary wave. An effective Ohnesorge number can thus be derived for the wave formation,

$$Oh_{\lambda} = \frac{\eta_{\infty}}{\sqrt{\rho \gamma \lambda}} = \frac{\eta_{\infty} U}{\gamma} = Ca_{\infty}.$$
 (5)

In Fig. 5(c), the variation of the apex height caused by the focusing of the capillary waves is normalized by the droplet radius, denoted as (H-Ut)/R, and illustrated with increasing Oh_{λ} . At $Oh_{\lambda}=0.44$, the top surface stopped oscillating, indicating the complete suppression of capillary waves. To elucidate how the infinite-shear viscosity modulates the wave formation, we consider the critical damping condition where the generation of waves at the interface ceases when the damping ratio

$$\xi_{cr} = \frac{\delta}{\omega_c} = 1,\tag{6}$$

where the damping coefficient δ is expressed as

$$\delta = \frac{2\eta_{\infty}(2\pi/\lambda)^2}{\rho} = \frac{8\pi^2\eta_{\infty}}{\lambda^2\rho},\tag{7}$$

and the oscillating frequency of the waves is given by

$$\omega_{\rm c} = \sqrt{\frac{\gamma (2\pi/\lambda)^3}{\rho} \tanh\left(\frac{2\pi R}{\lambda}\right)},\tag{8}$$

which depends on the droplet radius R and the wave number expressed by $2\pi/\lambda$. Given that the capillary wavelength is much smaller than the droplet size $(R \gg \lambda/2)$, the wave is assumed to

propagate on a deep pool, thus yielding $\tanh(2\pi R/\lambda)\approx 1$. Hence, the critical Ohnesorge number becomes

$$Ca_{\rm cr} = Oh_{\rm cr} = \frac{1}{2\sqrt{2\pi}} \approx 0.2. \tag{9}$$

Upon combining the above equations, wave generation is controlled by the Capillary number defined by $Ca_{\infty} = \eta_{\infty}U/\gamma$ and is suppressed beyond $Ca_{\rm cr} \approx 0.2$. Figure 5(d) demonstrates a good agreement between the experimental data and the theoretical prediction.

Now, we focus on the evolution of air layer morphology. The radial velocity of spreading droplets was measured by tracking the basal liquid–air interface via TIRM (see Fig. 6). To estimate the radial velocity of the escaped air, we measured U_a at the first minima $r=r_d$ with an averaged gap thickness $h_{\rm m}$ (see Fig. 6). Based on $U_a\approx U_dr_d/(2h_{\rm m}),^{29}$ we found that U_a was approximately one order of magnitude higher than U_r in the early stage of spreading [Fig. 7(a)]. As the droplet expanded toward the maximum spreading, U_a decreased. Following the top surface collapse at $t/t_{\rm ic}\approx 0.67$ after the maximum spreading, the air velocity accelerated due to the dimple inversion. Therefore, it is reasonable to expect the droplet basal plane to be sheared during the impact resulting from the large air escape velocities.

The initial dimple height of XG 250 ppm [\approx 3010 nm in Fig. 7(c)] exceeded G/W 78 wt. % (\approx 2590 nm) and Boger (\approx 2610 nm) droplets [see Figs. 7(b) and 7(d)] by 15.4%, indicating a lower stagnation pressure beneath shear-thinning droplets. Although G' of the Boger solution reaches 1 Pa at ω = 200 rad/s (Fig. 3), the elasto-capillary length, defined by $l_{\rm ec}$ = 3 γ/G' \approx 0.2 m, is nearly two orders of magnitude

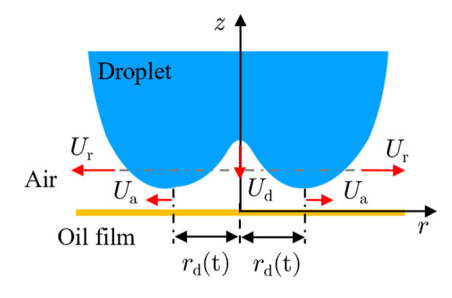


FIG. 6. A schematic of the air drainage. The red dashed line marks the upper limit (\approx 600 nm) of TIRM technique.

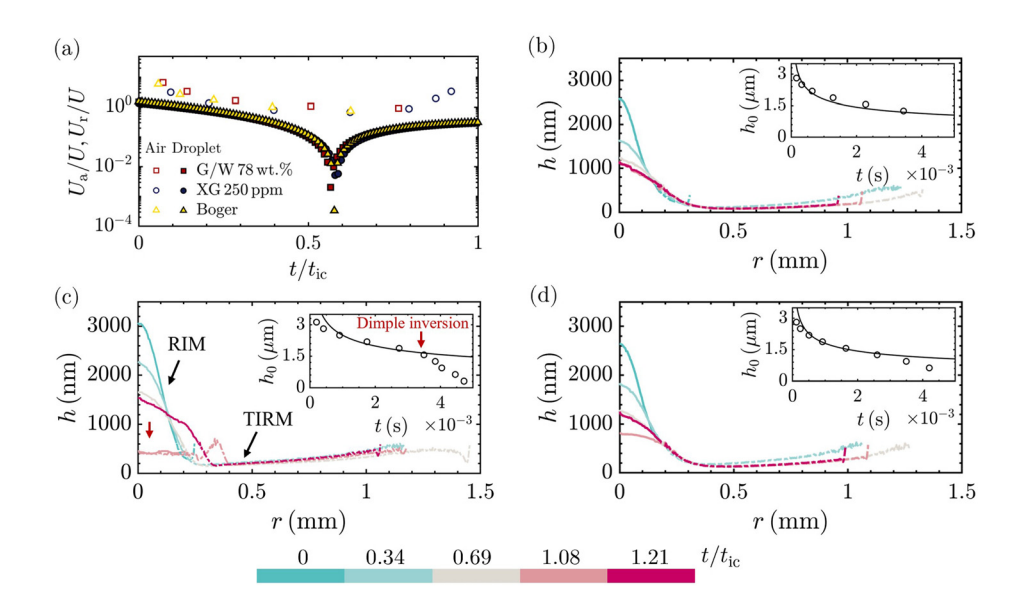


FIG. 7. (a) The radial velocity measurement of the basal plane of droplets and the escaping air underneath. Air layer height reconstructed from RIM (solid) and TIRM (dashed) measurements for (b) G/W 78 wt. %, (c) XG 250 ppm, and (d) Boger droplets, corresponding to droplet impact shown in Figs. 1(c)–1(e), respectively. Insets represent the dimple height variation (at r=0) over time. The solid line represents $h_0(t)=0.25t^{-1/3}$.

larger than the droplet size; therefore, elastic effects are regarded as negligible on the initial dimple height compared to capillarity for droplet impact at $O(0.1 \,\mathrm{m/s})$. Dimple height at r=0, denoted as h_0 , was tracked over time as shown in the insets [Figs. 7(b)-7(d)]. For incompressible airflow with its thickness $h \ll R$, and with the Reynolds number in the air, $Re_a \ll 1$, the variation of h is governed by the Stokes–Reynolds lubrication equation:

$$\frac{\partial h}{\partial t} = \frac{1}{12\eta_a} \frac{1}{r} \frac{\partial}{\partial r} \left(rh \frac{\partial p_a}{\partial r} \right), \tag{10}$$

where p_a is the driving pressure in the air layer and η_a is the viscosity of the air. The capillary pressure smoothens out the air dimple and takes over the drainage dynamics as described previously. Therefore, the driving pressure becomes $p_a = \gamma \partial^2 h/\partial r^2$, and the drainage rate follows $h_0 \sim t^{-1/3}$ for all three solutions before the collapsing top surface rapidly diminishes the dimple height of XG 250 ppm droplets after t=3.5 ms [Fig. 7(c)]. Moreover, although the impact velocity determines the initial dimple height, we also find that the power law governing the air drainage remains relatively insensitive to the Weber number (*We*) utilized in this study.

We next explore the accelerated drainage caused by the collapsing top surface. Since the top surface (reentrant jet) does not directly contact the air layer underneath the droplet—otherwise, wetting would be initiated—an intervening liquid film between the two must be highlighted, as depicted in Fig. 8(a), with a thickness of $H_{\rm sq}(t)=H_0(t)-h_0(t)$, which is much smaller than the lateral length. The thickness of the liquid film equals the droplet height prior to collapse and decreases rapidly as the top surface collapses downward (see Fig. 4). For the XG 250 ppm droplets, the dimple height decreases from 1.5 to 0.3 μ m within 1.25 ms caused by the pressure built up in the squeezing film, resulting in the inversion rate of approximately 1 mm/s, indicating $Re \ll 1$. Therefore, the lubrication approximation can again be considered to model the thin intervening liquid film between the reentrant jet and the air layer. We postulate that the lubrication pressure in this squeezing film must reach a critical value comparable to the gas pressure in the air layer to

invert the dimple. So, once the pressure in the squeezing film is established and surpasses the air pressure in the dimple, the inversion occurs and the dimple height decrease should follow a similar trend with the squeezing film thickness, $H_{\rm sq}(t) \sim h_0(t)$.

We now simplify the squeeze flow within the droplet to be flow between two parallel disks, which may be found for the Newtonian and power-law fluids in the following text. The film thickness h in Eq. (10) can thus be replaced with $H_{\rm sq}$ as well as the air viscosity with the viscosity of the intervening liquids η_0 . We start with the Newtonian case by integrating the pressure gradient in the squeezing film under the reentrant jet, it reproduces

$$p(r) = p_{\text{atm}} + \frac{3\eta_0 \left[-dH_{\text{sq}}(t)/dt \right] R_b^2}{H_{\text{sq}}^3(t)} \left[1 - \left(\frac{r}{R_b} \right)^2 \right], \quad (11)$$

where $p_{\rm atm}$ is the atmospheric pressure and R_b is the radius of the jet. Integrating the pressure in the z direction, we obtain the squeezing force exerted on the surfaces in the axial direction, which reads $3\eta_0\pi R_b^4[-dH_{\rm sq}(t)/dt]/[2H_{\rm sq}^3(t)]$. Integrating again over time, $H_{\rm sq}(t)$ can be expressed as

$$\frac{1}{H_{\rm sq}^2(t)} = \frac{1}{H_{\rm sq,0}^2} + \frac{4Ft}{3\pi\eta_0 R_{\rm b}^4},\tag{12}$$

where $H_{\rm sq,0}$ denotes the initial thickness of the squeeze film, and F denotes the applied force in the axial direction.

For the power law fluid with a power law index of *n*, the mass flow rate emerging from the thinning region becomes

$$\dot{m}(r) = \frac{\pi r H_{\text{sq}}^2(t)}{(1/n) + 2} \left[\frac{-dp(r)}{2dr} \frac{H_{\text{sq}}^{1/n}(t)}{\eta_0} \right]. \tag{13}$$

By equating the mass flow rate caused by the motion of the top surface and integrating the pressure gradient, the pressure distribution becomes

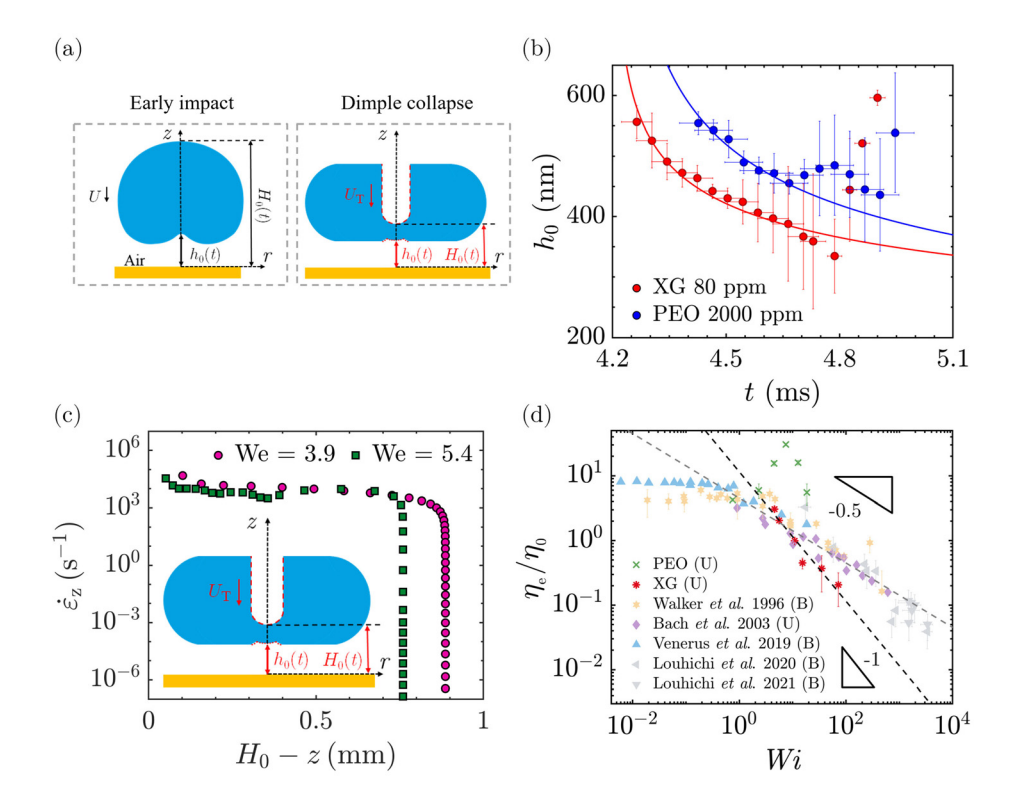


FIG. 8. (a) A schematic of dimple profile at early impact and the greatest collapse. (b) Time evolution of the distance (H) of the top surface from the substrate and the dimple height (h₀). (c) Strain rate of the collapsing top surface in the z direction for XG 250 ppm droplet. The inset provides a schematic of the reentrant jet. (d) Extensional viscosity normalized with zero shear viscosity over Wi, along with additional data from the literature.^{23,24,33–35} Extensional viscosity under uniaxial flows (droplet pinch-off) and biaxial flows (droplet top surface collapse) is presented separately.

$$p(r) = p_{\text{atm}} + \frac{2\eta_0 \left[-dH_{\text{sq}}(t)/dt \right] \left[(1/n) + 2 \right]^n R_{\text{b}}^{n+1}}{H_{\text{sq}}^{2n+1}(t)(n+1)} \left[1 - \left(\frac{r}{R_b} \right)^{n+1} \right]$$
(14)

which is the power-law equivalent of the Newtonian case and thus the variation of squeeze film thickness for the power law fluid is expressed by

$$\frac{1}{H_{\text{sq}}^{(1/n)+1}(t)} = \frac{1}{H_{\text{sq}0}^{(1/n)+1}} + \left[\frac{(1/n)+1}{(1/n)+2} \right] \left(\frac{n+3}{2\pi\eta_0 R_{\text{b}}^{n+3}} \right)^{1/n} F^{1/n} t. \quad (15)$$

With n = 1, Eq. (15) is simplified to Eq. (12) for the Newtonian fluid. As $n \to 0$, the film becomes easier to be thin under a constant force. Although it is difficult to measure the thickness of this squeeze film from either side or bottom views, we compare the dimple inversion dynamics of two non-Newtonian fluids XG 80 ppm (n = 0.26) and PEO 2000 ppm (n = 0.45) with a matched shear viscosity η_0 = 0.012mPas but different power law factors n. We set the initial dimple height as $h_0 = 3 \,\mu\text{m}$ and the radius $R_b = 0.3 \,\text{mm}$ of the cylindrical jet. The only varying parameter here was the force, F. As shown in Fig. 8(b), F = 0.0132 mN was obtained from the best fit for XG 80 ppm, whereas PEO 2000 ppm droplet required a stronger force of 0.0385 mN. This implies that an additional force in the axial direction is generated for the PEO solution during the collapse-induced dimple inversion, which may be ascribed to the higher first normal stress difference of the PEO under high shear rates. Notably, the force F applied for the two types of solution is of the same order of magnitude as the capillary force resulting from the reentrant jet, which is estimated by $F = 2\gamma R_{\rm b} \approx 0.036 \, {\rm mN}.$

In addition to the shear response, the extensional behavior of the surrounding flow of the reentrant jet may be evaluated by computing the strain rate in the z-direction based on $\dot{\varepsilon}_z = dH_0/(H_0dt)$. Also, the time-dependent extensional strain rate may be averaged as

$$\langle \bar{\dot{\varepsilon}}_z \rangle = \int_0^{H_0} (H_0 - z) \dot{\varepsilon}_z \, dz / \int_0^{H_0} (H_0 - z) \, dz,$$
 (16)

where we have found that $\langle \dot{\epsilon}_z \rangle$ varies between 10^5 and $0 \, s^{-1}$, as shown in Fig. 8(c) with an averaged value $\bar{\epsilon}_z \approx 18\,500 \pm 100 \, s^{-1}$.

Under such high strain rate, strain softening possibly contributes to the central collapse of the droplet at higher polymer concentrations. The influence of the strain softening on the extensional viscosity is estimated by plotting the Trouton ratio $\eta_{\rm e}/\eta_0$ over the Weissenberg number, $Wi=\tau\dot{\epsilon}$, as shown in Fig. 8(d), where τ is either the shear or extensional relaxation time, and the apparent uniaxial relaxation time $\tau_{\rm e}$ is applied for the PEO and XG solutions under uniaxial deformations. Generally, when Wi<1, $\eta_{\rm e}/\eta_0$ remains constant with values of 3 or 6 for uniaxial or biaxial flows, respectively. When Wi>1, molecules align with the flow direction, diminishing the resistance to the flow and possibly inducing strain softening at large strain rates.

For XG solutions, we estimate τ_e from Eq. (3), and the apparent uniaxial extensional viscosity is based on $2\eta(\dot{\gamma})/k$.³⁷ It is shown that for semi-rigid rod-like molecules such as XG at room temperature, the strain softening follows $\eta_e/\eta_0 \sim \langle \dot{\epsilon} \rangle^{-1}$. However, for PEO solutions, the strain softening follows $\langle \dot{\epsilon} \rangle^{-0.5}$, which agrees well with previous results of Louhichi *et al.*²³ The decrease in the softening rate was ascribed to the interchain pressure effects by Marrucci and Ianniruberto.³⁸ Specifically, as the concentrations enter an entangled regime, the polymers restate with diameter α , where its rate of change

scales as $\dot{\alpha} \sim -\dot{\epsilon}\alpha/2$. The tubes are free to stretch, and the diameters decrease. Such deformations allow internal pressure to build up against the compressive force, $\sigma_{\rm p} \approx v_{\rm m}k_{\rm B}Tb^2(\lambda_{\rm R}\dot{\epsilon})^{0.5}/l^2$, where $\tau_{\rm R}$ is the Rouse time, l is the blob size containing n monomers, $k_{\rm B}T$ is the thermal energy, and b is the tube length. The scaling for $\eta_{\rm e}/\eta_0 \sim \dot{\epsilon}^{-0.5}$ effectively captures the extensional thinning observed in polystyrene melts and entangled PEO solutions in previous studies. 23,24,34

For PEO solutions, the apparent uniaxial extensional viscosity was extracted from the stress balance within the elasto-capillary regime during pinch-off, $\eta_e = (\gamma/W)/\dot{\epsilon},^{25}$ where the apparent extensional relaxation time was estimated based from Eq. (2). We note that although PEO solutions manifest strain softening beyond $Wi \approx 10$, "strain hardening" is observed between 1 < Wi < 10. This increase in extensional viscosity is unlikely due to the chain stretch and possibly points to the skin formation of semicrystalline polymers like PEO, where the crystallization at the perimeter of the filament delays the thinning rate. ^{39,40} Nevertheless, we postulate that the strain softening may play a role in aiding the dimple inversion considering the large strain rate during the top surface collapse.

We show next the plot of the minimum air dimple height $h_{0[\min]}$ as a function of η_{∞} [Fig. 9 (top plot)]. Three distinct regimes were observed for PEO solutions and two distinct regimes for XG solutions. The first transition for both solutions is marked at $h_{0[\min]}=240$ nm. The corresponding η_{∞} can be related to the critical concentrations of the two solutions based on Fig. 9. For XG, $c^* \approx 100$ ppm and for PEO, $c^* \approx 400$ ppm. The second transition of PEO solutions is also

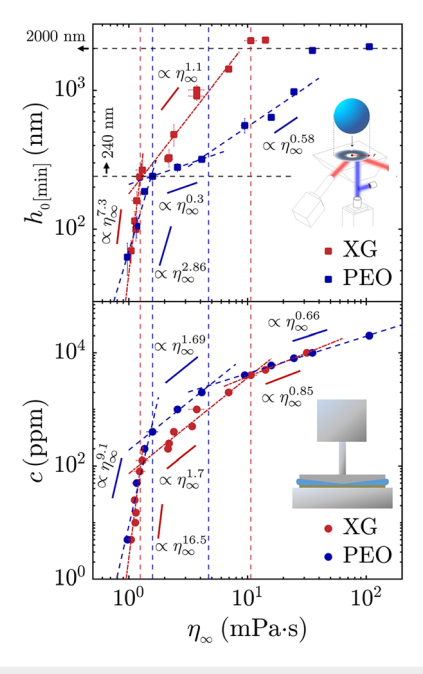


FIG. 9. Top plot: The minimum dimple height caused by the reentrant jet over the infinite-shear viscosity, η_{∞} . The two black dashed lines demonstrates the transitions from dilute to semi-dilute regimes $(h_{0[\min]}=240\,\mathrm{nm})$ and from semi-dilute to entangled regimes $(h_{0[\min]}=2000\,\mathrm{nm})$ for both XG and PEO solutions. Bottom plot: Critical concentrations, c^* and c^{**} , determined by the infinite-shear viscosity transitions over the concentration using the rheometer. The vertical dashed lines mark the critical transitions where red color highlights the XG solutions and blue highlights the PEO solutions.

indicative and predicts $c^* \approx 2400$ ppm. Notably, as the concentration increased, the dimple inversion was no longer detectable in our optics beyond the entangled regime.

To validate the accuracy of the droplet-based determination of critical concentrations, we predict the critical overlap concentration (c^*) using the semi-empirical expression:⁴¹

$$c^* \approx \frac{M_s}{N_A(R_g^3 \rho)},\tag{17}$$

where $N_{\rm A}$ is the Avogadro's constant, $M_{\rm s}$ is the polymer molecular weight, and $R_{\rm g}$ is the radius of gyration. The latter can be calculated through the Flory–Fox constant, $R_{\rm g}=0.41(M_{\rm s}[\eta]/\beta)^{1/3}$, where β varies with polymer structure, ranging from $2.86\times10^{23}\,{\rm mol}^{-1}$ for random coils to $1.36\times10^{25}\,{\rm mol}^{-1}$ for hard spheres. ⁴² For flexible linear chains like PEO in a good solvent, an accepted relation is shown by ^{43,44}

$$c^* = \frac{0.77}{[\eta]}. (18a)$$

Applying this to PEO with $[\eta]_{\rm PEO}=1900~{\rm cm}^3/{\rm g},^{45}$ the calculated c^* for PEO is approximately 410 ppm. For XG, characterized as a semirigid polymer, substituting $[\eta]_{\rm XG}=15\,500~{\rm cm}^3/{\rm g}^{46,47}$ into

$$c^* = \frac{1.45}{[\eta]} \tag{18b}$$

yields $c^* \approx 94$ ppm. While predicting the entangled critical concentration c^{**} remains challenging for semi-rigid polymer XG, where the droplet-determined $c^{**} \approx 1700$ ppm that exhibits 50% difference than the rheometer-determined $c^{**} \approx 2550$ ppm, our results provide a promising non-contact optical method for determining c^* and c^{**} using droplet impact whose predicted critical concentrations align well with rheometer-based measurements.

This study unravels the intricate interplay of shear and extensional effects in governing the capillary wave-assisted collapse of non-Newtonian droplets. Despite the initial appearance of biaxial flow during droplet spreading, shear effects surprisingly significantly impacted the dynamics. Capillary wave propagation was controlled by the Ca_{∞} , intricately linked to the infinite-shear viscosity of polymeric droplets. Large strain rates induced by the reentrant jet highlighted the role of strain softening in XG droplet collapse dynamics. Moreover, our work introduces an alternative way for determining the critical concentrations in aqueous polymer solutions through a rapid and cost-effective way by leveraging the physics of droplet impact.

ACKNOWLEDGMENTS

This work was financially supported by the National Science Foundation (No. 2137341). The authors thank Howard Stone and Paul R. Kaneelil for discussing the results and for their comments on the manuscript. Z.H. thanks Stanley Ling, Joseph Zasadzinski, Lynn M. Walker, Marufa Upoma, and Pooria Pirdavari for valuable discussions.

AUTHOR DECLARATIONS Conflict of Interest

The authors have no conflicts to disclose.

Author Contributions

Ziwen He: Data curation (equal); Formal analysis (equal); Investigation (equal); Methodology (equal); Software (equal); Validation (equal); Visualization (equal); Writing – original draft (equal); Writing – review & editing (equal). Huy Tran: Data curation (equal); Investigation (equal); Methodology (equal); Software (equal); Validation (equal); Visualization (equal); Writing – original draft (equal); Writing – review & editing (equal). Min Y. Pack: Conceptualization (equal); Data curation (equal); Formal analysis (equal); Funding acquisition (equal); Investigation (equal); Methodology (equal); Project administration (equal); Resources (equal); Software (equal); Supervision (equal); Validation (equal); Visualization (equal); Writing – original draft (equal); Writing – review & editing (equal).

DATA AVAILABILITY

The data that support the findings of this study are available from the corresponding author upon reasonable request.

REFERENCES

- ¹E. Turkoz, A. Perazzo, H. Kim, H. A. Stone, and C. B. Arnold, "Impulsively induced jets from viscoelastic films for high-resolution printing," Phys. Rev. Lett. 120, 074501 (2018).
- ²D. Lohse, "Fundamental fluid dynamics challenges in inkjet printing," Annu. Rev. Fluid Mech. 54, 349–382 (2022).
- ³X. Zhao, H. Cui, Y. Wang, C. Sun, B. Cui, and Z. Zeng, "Development strategies and prospects of nano-based smart pesticide formulation," J. Agric. Food Chem. **66**, 6504–6512 (2018).
- ⁴S. Bose, S. S. Keller, T. S. Alstrøm, A. Boisen, and K. Almdal, "Process optimization of ultrasonic spray coating of polymer films," Langmuir **29**, 6911–6919 (2013).
- ⁵J. Jiang, H. Zhang, W. He, T. Li, H. Li, P. Liu, M. Liu, Z. Wang, Z. Wang, and X. Yao, "Adhesion of microdroplets on water-repellent surfaces toward the prevention of surface fouling and pathogen spreading by respiratory droplets," ACS Appl. Mater. Interfaces 9, 6599–6608 (2017).
- ⁶M. A. Van Limbeek, M. H. K. Schaarsberg, B. Sobac, A. Rednikov, C. Sun, P. Colinet, and D. Lohse, "Leidenfrost drops cooling surfaces: Theory and interferometric measurement," J. Fluid Mech. 827, 614–639 (2017).
- ⁷J. C. Burton, A. L. Sharpe, R. C. A. van der Veen, A. Franco, and S. R. Nagel, "Geometry of the vapor layer under a Leidenfrost drop," Phys. Rev. Lett. 109, 074301 (2012).
- ⁸J. de Ruiter, J. M. Oh, D. van den Ende, and F. Mugele, "Dynamics of collapse of air films in drop impact," Phys. Rev. Lett. **108**, 074505 (2012).
- ⁹J. M. Kolinski, S. M. Rubinstein, S. Mandre, M. P. Brenner, D. A. Weitz, and L. Mahadevan, "Skating on a film of air: Drops impacting on a surface," Phys. Rev. Lett. **108**, 074503 (2012).
- ¹⁰M. Shirota, M. A. J. van Limbeek, C. Sun, A. Prosperetti, and D. Lohse, "Dynamic Leidenfrost effect: Relevant time and length scales," Phys. Rev. Lett. 116, 064501 (2016).
- ¹¹M. Y. Pack, A. Yang, A. Perazzo, B. Qin, and H. A. Stone, "Role of extensional rheology on droplet bouncing," Phys. Rev. Fluids 4, 123603 (2019).
- ¹²Z. He, H. Tran, and M. Y. Pack, "Air entrainment dynamics of aqueous polymeric droplets from dilute to semidilute unentangled regimes," Phys. Fluids 34, 113105 (2022).
- ¹³Z. He, M. A. Upoma, and M. Y. Pack, "Dual nature of volatility on drop wetting dynamics of acetone-isopropanol mixtures on ultrathin smooth oil films," Phys. Fluids 35, 012115 (2023).
- ¹⁴M. Pack, H. Hu, D. Kim, Z. Zheng, H. A. Stone, and Y. Sun, "Failure mechanisms of air entrainment in drop impact on lubricated surfaces," Soft Matter 13, 2402–2409 (2017).
- ¹⁵Y. Renardy, S. Popinet, L. Duchemin, M. Renardy, S. Zaleski, C. Josserand, M. Drumright-Clarke, D. Richard, C. Clanet, and D. Quéré, "Pyramidal and

- toroidal water drops after impact on a solid surface," J. Fluid Mech. 484, 69–83 (2003).
- 16B. Zhang, V. Sanjay, S. Shi, Y. Zhao, C. Lv, X.-Q. Feng, and D. Lohse, "Impact forces of water drops falling on superhydrophobic surfaces," Phys. Rev. Lett. 129, 104501 (2022).
- ¹⁷D. Bartolo, C. Josserand, and D. Bonn, "Singular jets and bubbles in drop impact," Phys. Rev. Lett. 96, 124501 (2006).
- ¹⁸V. Bergeron, D. Bonn, J. Y. Martin, and L. Vovelle, "Controlling droplet deposition with polymer additives," Nature 405, 772–775 (2000).
- ¹⁹D. Bartolo, A. Boudaoud, G. Narcy, and D. Bonn, "Dynamics of non-Newtonian droplets," Phys. Rev. Lett. 99, 174502 (2007).
- Newtonian dropiets, Phys. Rev. Lett. 93, 174502 (2007).
 M. I. Smith and V. Bertola, "Effect of polymer additives on the wetting of impacting droplets," Phys. Rev. Lett. 104, 154502 (2010).
- ²¹V. Bertola, "Effect of polymer concentration on the dynamics of dilute polymer solution drops impacting on heated surfaces in the Leidenfrost regime," Exp. Therm. Fluid Sci. 52, 259–269 (2014).
- ²²A. Rozhkov, B. Prunet-Foch, and M. Vignes-Adler, "Impact of drops of polymer solutions on small targets," Phys. Fluids 15, 2006–2019 (2003).
- ²³A. Louhichi, C.-A. Charles, T. Phou, D. Vlassopoulos, L. Ramos, and C. Ligoure, "Biaxial extensional viscous dissipation in sheets expansion formed by impact of drops of Newtonian and non-Newtonian fluids," Phys. Rev. Fluids 5, 053602 (2020).
- ²⁴A. Louhichi, C.-A. Charles, S. Arora, L. Bouteiller, D. Vlassopoulos, L. Ramos, and C. Ligoure, "Competition between shear and biaxial extensional viscous dissipation in the expansion dynamics of Newtonian and rheo-thinning liquid sheets," Phys. Fluids 33, 073109 (2021).
- ²⁵J. Dinic, Y. Zhang, L. N. Jimenez, and V. Sharma, "Extensional relaxation times of dilute, aqueous polymer solutions," ACS Macro Lett. 4, 804–808 (2015).
- ²⁶S. Lakshman, W. Tewes, K. Harth, J. H. Snoeijer, and D. Lohse, "Deformation and relaxation of viscous thin films under bouncing drops," J. Fluid Mech. 920, A3 (2021).
- ²⁷K. W. Ebagninin, A. Benchabane, and K. Bekkour, "Rheological characterization of poly (ethylene oxide) solutions of different molecular weights," J. Colloid Interface Sci. 336, 360–367 (2009).
- ²⁸V. Entov and E. Hinch, "Effect of a spectrum of relaxation times on the capillary thinning of a filament of elastic liquid," J. Non-Newtonian Fluid Mech. **72**, 31–53 (1997).
- ²⁹R. C. A. van der Veen, T. Tran, D. Lohse, and C. Sun, "Direct measurements of air layer profiles under impacting droplets using high-speed color interferometry," Phys. Rev. E 85, 026315 (2012).
- 30 S. Arora, J.-M. Fromental, S. Mora, T. Phou, L. Ramos, and C. Ligoure, "Impact of beads and drops on a repellent solid surface: A unified description," Phys. Rev. Lett. 120, 148003 (2018).
- ⁵¹D. Y. Chan, E. Klaseboer, and R. Manica, "Film drainage and coalescence between deformable drops and bubbles," Soft Matter 7, 2235–2264 (2011).
- ³²W. Bouwhuis, R. C. A. van der Veen, T. Tran, D. L. Keij, K. G. Winkels, I. R. Peters, D. van der Meer, C. Sun, J. H. Snoeijer, and D. Lohse, "Maximal air bubble entrainment at liquid-drop impact," Phys. Rev. Lett. 109, 264501 (2012).
- 33L. M. Walker, P. Moldenaers, and J.-F. Berret, "Macroscopic response of worm-like micelles to elongational flow," Langmuir 12, 6309–6314 (1996).
- 34A. Bach, K. Almdal, H. K. Rasmussen, and O. Hassager, "Elongational viscosity of narrow molar mass distribution polystyrene," Macromolecules 36, 5174– 5179 (2003).
- 35D. C. Venerus, R. M. Mick, and T. Kashyap, "Equibiaxial elongational rheology of entangled polystyrene melts," J. Rheol. 63, 157–165 (2019).
- ³⁶R. B. Bird, W. E. Stewai, and E. N. Lightfoot, *Transport Phenomena*, 2nd ed. (John Wiley & Sons, Inc., New York, 2006).
- ³⁷R. Larson and H. Brenner, Constitutive Equations for Polymer Melts and Solutions: Butterworths Series in Chemical Engineering (Elsevier Science, 2013).
- ³⁸G. Marrucci and G. Ianniruberto, "Interchain pressure effect in extensional flows of entangled polymer melts," <u>Macromolecules</u> 37, 3934–3942 (2004).
- ³⁹D. R. Paul, "Diffusion during the coagulation step of wet-spinning," J. Appl. Polym. Sci. 12, 383–402 (1968).
- 40 R. H. Colby, "Fiber spinning from polymer solutions," J. Rheol. 67, 1251–1255
- ⁴¹W. W. Graessley, "Polymer chain dimensions and the dependence of viscoelastic properties on concentration, molecular weight and solvent power," Polymer 21, 258–262 (1980).

- ⁴²A. Lederer, W. Burchard, A. Khalyavina, P. Lindner, and R. Schweins, "Is the universal law valid for branched polymers?," Angew. Chem. Int. Ed. **52**, 4659– 4663 (2013).
- ⁴³C. Clasen, J. Plog, W.-M. Kulicke, M. Owens, C. Macosko, L. Scriven, M. Verani, and G. H. McKinley, "How dilute are dilute solutions in extensional flows?," J. Rheol. **50**, 849–881 (2006).
- ⁴⁴W. C. Smith, H. Qu, K. Zheng, J. H. Baek, Y. Gao, P. W. Buehler, X. Feng, and X. Xu, "Determining critical overlap concentration of polyethylene oxide to support excipient safety assessment of opioid products," Int. J. Pharm. 632, 122557 (2023).
- ⁴⁵A. Dupas, I. Hénaut, J.-F. Argillier, and T. Aubry, "Mechanical degradation onset of polyethylene oxide used as a hydrosoluble model polymer for enhanced oil recovery," Oil Gas Sci. Technol. 67, 931–940 (2012).
- enhanced oil recovery," Oil Gas Sci. Technol. 67, 931–940 (2012).

 46H. Khouryieh, T. Herald, F. Aramouni, and S. Alavi, "Intrinsic viscosity and viscoelastic properties of xanthan/guar mixtures in dilute solutions: Effect of salt concentration on the polymer interactions," Food Res Int. 40, 883–893 (2007).
- ⁴⁷T. Rodrigues, F. J. Galindo-Rosales, and L. Campo-Deaño, "Critical overlap concentration and intrinsic viscosity data of xanthan gum aqueous solutions in dimethyl sulfoxide," Data Brief 33, 106431 (2020).